Accepted Manuscript

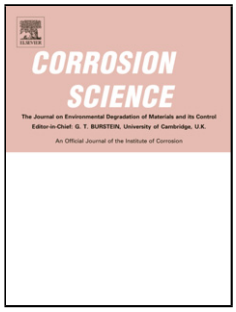

Title: The influence of hydrogen on the mechanical and fracture properties of some martensitic advanced high strength steels studied using the linearly increasing stress test

Author: Jeffrey Venezuela Qinglong Liu Mingxing Zhang Qingjun Zhou Andrej Atrens

PII: S0010-938X(15)00329-7
DOI: http://dx.doi.org/doi:10.1016/j.corsci.2015.06.038
Reference: CS 6396

To appear in:

Received date: 13-3-2015
Revised date: 22-6-2015
Accepted date: 25-6-2015

Please cite this article as: Jeffrey Venezuela, Qinglong Liu, Mingxing Zhang, Qingjun Zhou, Andrej Atrens, The influence of hydrogen on the mechanical and fracture properties of some martensitic advanced high strength steels studied using the linearly increasing stress test, Corrosion Science http://dx.doi.org/10.1016/j.corsci.2015.06.038

The influence of hydrogen on the mechanical and fracture properties of some martensitic advanced high strength steels studied using the linearly increasing stress test

Jeffrey Venezuela[1], Qinglong Liu[1], Mingxing Zhang[1], Qingjun Zhou[2], Andrej Atrens[1,*]

[1] The University of Queensland, Division of Materials, School of Mining and Mechanical Engineering, St. Lucia, 4072 Australia

[*] Corresponding author, andrejs.atrens@uq.edu.au

[2] Baoshan Iron & Steel Co., Ltd, Research Institute, Shanghai, 201900,China

Highlights

Hydrogen influence increased with strength, charging potential, and decreasing applied stress rate.

The hydrogen influence was manifest by reduced strength, changed fracture and decreased ductility.

The decrease in yield stress was attributed to solid solution softening by hydrogen

Hydrogen caused a change at the fracture stress when the specimen was mechanically unstable

The fracture changed from ductile cup-and-cone fracture to macroscopically brittle shear fracture.

ABSTRACT

The influence of hydrogen on the mechanical and fracture properties of four martensitic advanced high strength steels was studied using the linearly increasing stress test and electrochemical hydrogen charging. The hydrogen influence increased with steel strength, decreasing charging potential, and decreasing applied stress rate. Increased hydrogen

influence was manifest in (i) the decreased yield stress attributed to solid solution softening by hydrogen and (ii) the reduced macroscopic ductility, and by the change from ductile cup-and-cone fracture to macroscopically brittle shear fracture, attributed to a dynamic interaction of hydrogen with the dislocation substructure somewhat similar to the HELP mechanism.

Keywords: A. steel; B. SEM; C. hydrogen embrittlement

1. INTRODUCTION

Advanced high strength steels (AHSS) are new steels created for the automotive industry [1-4] to decrease vehicle weight, and an improve vehicle crash resistance [4]. AHSS differ from conventional auto steels in that they have higher strength, typically greater than 600 MPa, and often between 800 to 1200 MPa [5]. This higher strength is achieved by relatively complex metallurgy. Research on AHSS began in the early 1980s, and led to the creation of the first-generation AHSS [6, 7]. These AHSS were ferrite-based, and examples include dual-phase (DP), martensitic (MS), complex phase (CP) and transformation-induced plasticity (TRIP) steels [8]. Subsequent research is developing the third-generation AHSS [8-10].

The martensitic AHSS (MS-AHSS) are the strongest, but exhibiting the lowest ductility [11]. Strength and hardness increase with increasing carbon content, whereas the ductility and toughness decrease with increasing carbon content. The lack of ductility also limits formability of these steels, which is important, because auto bodies are mechanically shaped from sheet steel. Nevertheless, MS-AHSS are important because they have the highest strength-to-price ratio among AHSS [8]. MS-AHSS find applications in the parts of the vehicle which require good crash resistance, such as bumper beams and reinforcements, door intrusion beams and reinforcements, windscreen upright reinforcements, and B-pillar reinforcements [1, 12-14].

Hydrogen embrittlement (HE) has long been the bane of high-strength steels [15-17]. HE is a failure mode caused by the presence of a relatively small amount of hydrogen. HE may trigger catastrophic failures at relatively-small applied loads, or may cause degradation of ductility and toughness. Recent studies have revealed some HE susceptibility for some

AHSS [18-22]. However, past attempts to predict HE resistance based on the microstructure, composition and processing, have not been successful. Hence, a much deeper understanding of how hydrogen interacts with steel is essential to reduce or eliminate HE in AHSS.

Several mechanisms have been proposed for HE. For non-hydride forming metals such as steel, the following three mechanisms are the most likely: (i) hydrogen-enhanced decohesion (HEDE), (ii) hydrogen-enhanced local plasticity (HELP), and (iii) adsorption-induced dislocation emission (AIDE) [16]. The HEDE mechanism proposes that hydrogen causes a reduction in the cohesive bond strength between metal atoms, leading to weakness under tensile load, and causing brittle crack propagation [23, 24]. The HELP mechanism proposes that the presence of hydrogen increases dislocation mobility, causing highly localized plastic deformation [25]. Since the plastic deformation is concentrated in a small volume, the total macroscopic ductility is low. The HELP mechanism has considerable support [15, 26, 27], even though, at first blush, the terms enhanced plasticity and embrittlement appear contradictory. The AIDE mechanism is similar to the HELP mechanism, in that AIDE also involves localized plasticity. The key difference is that AIDE proposes that the localised plasticity occurs close to the surface. The AIDE mechanism proposes that hydrogen is adsorbed at the surface, at regions of stress concentrations like crack tips [28], and that the hydrogen triggers the release of dislocations from the advancing crack tip, causing crack growth, and intense deformation in the crack vicinity.

The linearly increasing stress test (LIST), was developed by Atrens et al. [29] for the study of HE and stress corrosion cracking (SCC). The LIST subjects a smooth specimen to a linearly increasing load until the specimen fractures [30]. The specimen may be tested in air, or when exposed to an embrittling environment. The LIST is load controlled, whereas the related constant extension rate test (CERT) is strain controlled. Both tests are identical until yielding, or the initiation of sub-critical cracking. Thereafter, the LIST is concluded more rapidly, whereas a considerable length of time is taken in a CERT, whilst cracks open up relieving the applied strain, and the specimen extends. Winzer et al [31] showed that both tests can provide similar information, if instrumented, to evaluate the threshold stress for crack initiation by HE or SCC, although CERTs are rarely so instrumented. The LIST has been successfully applied to different types of steels, such as plain carbon [32, 33], alloy [33, 34], micro-alloyed [33, 35], high strength [33, 36], and medium strength steels [37, 38]. To the knowledge of the authors, there has been no investigation of the influence of hydrogen on the mechanical properties of MS-AHSS using the LIST.

In summary, LIST has the following advantages. The LIST allows measurement of the yield stress and the threshold stress for crack initiation by hydrogen or by stress corrosion cracking. This quantity is potentially a design allowable, which could be used in the assessment of structural integrity of a component in service. This also allows quantification of the degree of hydrogen influence in terms of the reduction of the threshold stress, as well as in terms of the decrease in ductility. Furthermore, the LIST is considerably quicker than a CERT at the same applied stress rate.

The aims of the present work were: (i) to investigate the influence of hydrogen on the mechanical properties (particularly the threshold stress for crack initiation and the ductility) and fracture processes of four commercial martensitic AHSS, (ii) identify the mechanisms of HE involved in each fracture process, and (iii) determine the environmental limits of the usability of these steels.

2.0 EXPERIMENTAL METHODOLOGY

2.1 Steels

The four martensitic AHSS were commercially produced, in the form of rolled-sheet. The four steel grades were given the following designations: MS980, MS1180, MS1300, and MS1500. The mean sheet thicknesses were 1.2 mm for MS1300 and MS1500, 1.5 mm for MS980, and 1.8 mm for MS1180. Table 1 presents the chemical and mechanical properties of the steels, as provided by the steel producer. From MS980 to MS1500, the yield and tensile strengths increased, the ductility decreased, there was a slight increase in the carbon content, and the concentration of the other alloying elements was essentially constant.

2.2. Microstructure analysis

Representative samples were metallurgically mounted using a conductive polymer resin; ground using a series of emery or silicon carbide (SiC) papers starting from 300 grit, followed with 600 grit, and finishing with 1200 grit paper; rough polished using 3 and 1 μm diamond; final polished using colloidal silica; etched with 2% nital, and viewed with a light microscope (LM), and with a scanning electron microscope (SEM). The microstructure of each steel consisted mainly of ferrite and martensite. The relative amounts of each phase

were evaluated using point analysis as described in ASTM E562 [39]. The grain size was estimated using the microscope calibration bar.

2.3. Linearly Increasing Stress Tests (LISTs)

Fig. 1 presents a typical LIST specimen. The specimen thickness corresponded to the steel sheet thickness. These specimens were machined from the steel sheet, and polished with 1200 grit SiC paper. The long direction of the specimen coincided with the rolling direction of the steel sheet.

Fig. 2 presents a schematic of the LIST apparatus [29]. The loading train for the specimen was on the left hand side of the lever beam. This allowed the specimen to be exposed to the environment. A 14 kg weight, on the other side, was moved, starting at the equilibrium position, along the lever beam by a synchronous motor, and resulted in the application of a linearly increasing (engineering) stress to the specimen. The applied (engineering) stress on the specimen was given by [29]:

$$s = \frac{(13720)d}{A} \tag{1}$$

where d (m) was the position of the movable weight from the zero load condition, and A was the specimen cross-section area (mm^2) of the gauge section. The numerical factor in Eq (1) depended on the mechanical advantage, the mass of the movable weight (14 kg) and g, the acceleration due to gravity. The applied stress rate could be specified by the choice of the synchronous motor driving the weight from the equilibrium position.

LISTs were carried out in laboratory air, and with electrochemical cathodic charging at -1.200, -1.500 and -1.800 $V_{Ag/AgCl}$ in a 0.1 M NaOH (pH 12.6) solution. Increasingly negative potentials represent increasing hydrogen fugacity. The electrochemical charging was carried out using a typical three-electrode cell as shown schematically in Fig. 3. The LIST sample was the working electrode, the counter electrode was a platinum mesh, and the reference electrode was Ag/AgCl saturated with KCl. The applied cathodic potential was controlled using a Bank Electronik MP81 potentiostat. The solution was prepared using analytic grade reagent and distilled water.

Before each LIST, to ensure an equilibrium and constant hydrogen content throughout the specimen, the specimen was hydrogen pre-charged at the charging potential in the 0.1 M NaOH solution for 24 h, with a static stress of 20% of the yield strength applied to the specimen.

The applied stress rates on the samples varied according to the speed of the synchronous motor. Three motors were used with speeds of 3, 30 and 300 revolutions per hour (rph). The 300-rph motor produced the fastest applied stress rate, the 30-rph motor produced the intermediate rate, and 3-rph motor produced the slowest rate. The applied stress rates depended also on the specimen dimensions. The 300-rph motor produced applied stress rates of 0.54, 0.64, and 0.8 MPa s^{-1}, the 30 rph motor produced applied stress rates of 0.054, 0.064, and 0.08 MPa s^{-1}, and the 3 rph motor produced applied stress rates of 0.0054, 0.0064, and 0.008 MPa s^{-1}. An applied stress rate of 0.8 MPa s^{-1} corresponds to a strain rate of 3.9 x 10^{-6} s^{-1} in the initial elastic part of the Linearly Increasing Stress Test (LIST), whereas an applied stress rate of 0.0054 MPa s^{-1} corresponds to a strain rate of 2.6 x 10^{-8} s^{-1} in the initial elastic part of the LIST.

The specimen designation indicated the type of steel, the environment, and the speed of the synchronous motor, which provided an indication of the applied stress rate. Thus, the sample designation ‘MS980-A-300’ indicated MS980 steel, tested in air, using the 300-rph-synchronous motor. The mechanical properties related to the specimens designated as ‘XXXX-A-S’ in Table 3 were measured using an universal tensile testing machine by the steel supplier at a strain rate faster than that of the applied stress rate corresponding to the fastest synchronous motor (i.e. 300 rph) used in the LISTs.

The LISTs were used to evaluate the apparent threshold stress for the initiation of subcritical crack growth in the hydrogen-charged samples, σ_{TH}, or the yield stress for the uncharged sample, σ_y, the fracture stress, σ_f, and the reduction in area, R_A. A direct current potential drop (DCPD) technique was used to evaluate σ_{TH} and σ_y, as described by Atrens et al [29]. A 3-ampere stabilized direct current was applied to the specimen, and the potential drop across the specimen gauge length was measured. This is equivalent to measuring the change in resistance, given by:

$$\Delta R = \frac{\rho L}{\Delta A} \quad (2)$$

where ΔA was the change in cross-sectional area, ρ was the resistivity, L was the apparent gauge length of the specimen. As the stress increased, the potential drop initially increased slowly because of the decrease in specimen area, and the increase in specimen length. At the onset of subcritical crack growth, there was a greater rate of decrease in specimen cross-section, and the potential drop increased more quickly. A plot of potential drop vs the applied stress thus increased relatively slowly until the start of sub-critical crack growth, whereupon the slope increased significantly. The same type of change in specimen resistance also occurred during plastic yielding of the sample. Thus, the stress at this change in slope corresponded to either σ_{TH} or σ_y. Fractography was required to identify the quantity as corresponding to a yield stress or a threshold stress for sub-critical crack initiation. The precision for the evaluation of σ_{TH} or σ_y was ± 5 MPa, whilst the precision for σ_F was ± 2 MPa.

The degree of hydrogen influence was quantified using (i) the hydrogen susceptibility index, S_H, related to the decrease in the threshold stress and (ii) the hydrogen embrittlement index, I, related to the decrease in ductility, as proposed by Loidl et al [21]). The hydrogen susceptibility index, S_H, was evaluated as follows:

$$S_H = \frac{T_{air} - T_H}{T_{air}} 100\% \quad (3)$$

where T_{air} is the yield stress in air, and T_H is the apparent threshold stress in the hydrogen charging environment. The value of the susceptibility index, S_H, may vary from 0% to 100%, from no hydrogen influence to high influence. The hydrogen embrittlement index, I, was evaluated as follows:

$$I = \frac{R_{A,air} - R_{A,H}}{R_{A,air}} 100\% \quad (4)$$

where $R_{A,air}$ is the reduction in area in air, and $R_{A,H}$ is the reduction in area in the hydrogen charging environment. The value of the embrittlement index, I, may also vary from 0% to 100%, from no hydrogen embrittlement susceptibility to high embrittlenment.

2.4. Fractography

The fracture surfaces were cut, using an alumina saw, to an appropriate size for SEM examination. Each specimen was cleaned in EDTA solution followed by ultrasonic cleaning for 30 minutes in a hot 4% Alconox solution [40]. These samples were then blow-dried, mounted onto an aluminium stub using conductive carbon tape, and examined using the JEOL 6610 SEM.

3. RESULTS

3.1. Metallurgy

Fig. 4a presents typical views of the microstructure of the MS-AHSS as revealed by optical microscopy. The microstructure of each steel consisted mainly of ferrite and martensite.

Table 2 presents (i) the relative amounts of each phase and (ii) the grain size. The amount of martensite increased from MS980 to MS1500, whilst the amount of ferrite decreased. The martensite grain size was similar for all the steels and was larger than the size of the ferrite grains. However, the grain size attributed to martensite in these measurements is likely the size of prior austenite grains (PAG). The microstructure of martensite is complex and possesses different levels of organization such as laths, packets and blocks [41]. Laths are the finest of these structures. A packet may be considered as a single martensite grain, though partitioned by many low-angle lath boundaries, and having a dense dislocation population [42]. Unfortunately, packets are difficult to distinguish in the etched microstructure, and thus the reliance on the PAG size, which is easily discernible.

Fig. 4b presents the two-phase microstructures as revealed by SEM. The martensite appeared rough and embossed, whilst the ferrite showed a dark smooth surface. Etching also revealed the needle-like or acicular structure characteristic of martensite. Furthermore, the ferrite appeared deeper or at a lower level than the martensite grains.

3.2. Mechanical properties

Fig. 5 presents typical potential drop data for the determination of σ_{TH}, determined as the transition stress corresponding to a significant increase in the slope.

Table 3 and Fig. 6 presents the LIST results. The values of yield stress, $\sigma_{y,}$ and tensile stress, σ_F, for each steel evaluated using LISTs in air were in good agreement with the

corresponding values measured using conventional tensile tests by the steel supplier as presented in Table 1. There might be a slight decrease in strength with decreasing stress rate as is evident by comparing the strength values in air for MS1300 specimens tested in air at 0.8, 0.08 and 0.008 MPa s^{-1}. However, this trend was not present in all cases, and may simply indicate that the experimental error due to inter-specimen variability was somewhat larger than the precision of the measurements.

Table 3 indicates that, for MS980, at an applied stress rate of 0.064 MPa s^{-1}, the values of σ_{TH}, σ_F and R_A were similar to the corresponding values measured in air, for all values of the cathodic charging potential. At an applied stress rate of 0.0064 MPa s^{-1}, the LIST values for the specimen charged at -1.200 $V_{Ag/AgCl}$ and -1.500 $V_{Ag/AgCl}$ were similar to those for the uncharged specimen. However, the specimen charged at -1.800 $V_{Ag/AgCl}$ showed a decrease in the values of σ_{TH}, σ_F and R_A.

Figs. 6a and 6b indicate that, for MS980, there was a small decrease in the relative yield stress and a small increase in hydrogen susceptibility index respectively, both of which effects became larger with decreasing applied stress rate, and were larger for a hydrogen charging potential of -1.800 $V_{Ag/AgCl}$ compared with the values at -1.200 $V_{Ag/AgCl}$. In contrast, Figs. 6c and 6d indicate that the hydrogen embrittlement index was zero for MS980 at an applied stress rate of 0.064 MPa s^{-1}, for all values of the cathodic charging potential, whereas the hydrogen embrittlement index was small but increased with increasingly negative charging potential at an applied stress rate of 0.0064 MPa s^{-1}.

Table 3 indicates that the results for MS1180 were similar to those for MS980. At an applied stress rate of 0.054 MPa s^{-1}, the values of σ_{TH}, σ_F and R_A were similar to the corresponding values measured in air, for all values of cathodic charging potential, except that the value of R_A was about 18% lower for the specimen tested at -1.800 $V_{Ag/AgCl}$. At the lower applied stress rate of 0.0054 MPa s^{-1}, the specimen charged at -1.500 $V_{Ag/AgCl}$ and -1.800 $V_{Ag/AgCl}$ showed a significant decrease in the values of σ_{TH}, σ_F and R_A.

Figs. 6a and 6b indicate that, for MS1180, there was also a small decrease in the relative yield stress and also a small increase in the hydrogen susceptibility index, both of which effects became larger with decreasing applied stress rate, and were larger for a hydrogen charging potential of -1.800 $V_{Ag/AgCl}$ compared with the values at -1.200 $V_{Ag/AgCl}$. In contrast, Figs. 6c and 6d indicate that the hydrogen embrittlement index was small for

MS1180 at an applied stress rate of 0.054 MPa s^{-1}, for cathodic charging potentials of -1.200 $V_{Ag/AgCl}$ and -1.500 $V_{Ag/AgCl}$, and was substantial for the cathodic charging potential of -1.800 $V_{Ag/AgCl}$, whereas the hydrogen embrittlement index was larger and increased with increasingly negative charging potential at an applied stress rate of 0.0054 MPa s^{-1}.

Table 3 and Fig. 6 indicate that MS1300 and MS1500 displayed significant hydrogen susceptibility at the higher stress rate (i.e. 0.08 MPa s^{-1}) at all charging conditions. Therefore, at the lower stress rate the samples were only exposed to most severe charging potential of -1.800 $V_{Ag/AgCl}$, with the expectation of observing the worst extent of the hydrogen influence. For MS1300, at an applied stress rate of 0.08 MPa s^{-1}, $\sigma_{TH,}$ σ_F and R_A were reduced at each cathodic charging potential. The amount of reduction increased with increasingly negative cathodic charging potential. For example, a comparison between MS1300-A-30, the uncharged sample, and MS1300-1.8-30, the sample charged at the most negative cathodic charging potential of -1.800 $V_{Ag/AgCl}$, indicated that (i) σ_F decreased by 4%, from 1436 MPa to 1388 MPa, (ii) σ_{TH} decreased by 10%, from 1160 MPa to 1075 MPa, and (iii) R_A decreased by 53% from 62% to 29%. Furthermore, at the slower rate of 0.008 MPa s^{-1}, $\sigma_{TH,}$ σ_F and R_A were reduced further, as is evident by comparing MS1300-1.8-30 and MS1300-1.8-3. For MS1500, the trends were the same as for MS1300. At an applied stress rate of 0.08 MPa s^{-1}, $\sigma_{TH,}$ σ_F and R_A were reduced at each cathodic charging potential. The amount of reduction increased with increasingly negative cathodic charging potential. Furthermore, at the slower rate of 0.008 MPa s^{-1}, $\sigma_{TH,}$ σ_F and R_A were reduced further.

Table 3 and Fig. 6 include data for the hydrogen susceptibility index, S_H, and the embrittlement index, I. MS980 and MS1180 steels had (i) zero or low S_H and I values at intermediate applied stress rates, and (ii) moderate values at the lowest applied stress rate, at which MS1180 showed substantial increases in S_H and I at -1.500 $V_{Ag/AgCl}$ and -1.800 $V_{Ag/AgCl}$. There were significant S_H and I values for the two strongest grades, MS1300 and MS1500, which increased with increasingly negative cathodic charging potential. Furthermore, the S_H and I values were higher at the slowest applied stress rate.

3.3 Fractography at the intermediate stress rates

3.3.1 Typical fractures

Tables 3 and 4 include a summary of the observations of the fracture behaviour of the MS-AHSSs. The fractures were classified into two types: (i) cup-and-cone, and (ii) shear-type fracture.

Figs. 7 and 8 illustrate typical cup-and-cone fractures. Fig. 7a presents the top view, indicating significant necking, as is also evident from the view from the transverse side, Fig. 7b, and the short transverse side, Fig. 7c. Specimens with this fracture type had high values of R_A, consistent with ductile behaviour. Cup-and-cone fractures occurred for (i) all four steels tested in air (MS980, MS1180, MS1300, and MS1500), and (ii) for MS980 and MS1180 tested under hydrogen charging conditions at the three potentials, and at 0.064 and 0.054 MPa s^{-1}, respectively. Fig. 8a presents a view normal to the fracture surface, and illustrates that the cup-and-cone fracture possessed two distinct regions: (i) the central region, marked A, and (ii) the shear lips, marked B. The central region showed a rough topography. The fracture surface was flat, and oriented perpendicular to the tensile direction. This central region consisted of round microvoid dimples, as illustrated by a typical example in Fig. 8b, at higher magnification. The shear lips occurred between the central region and the specimen edge. The surface appeared smooth, was sloping in relation to the flat core, and was typically at 45° to the tensile stress. Fig. 8c illustrates that, at higher magnification, the surface possessed shallow parabolic depressions characteristic of shear dimples.

Fig. 9 presents some typical examples of the shear-type fracture. The angle of the fracture was about 45^o to the direction of the applied tensile stress, which was vertical in these figures. In some cases, the shear fracture was essentially all in a single plane, such as in Fig 9a. In other cases, the fracture appeared blocky, and involved shear on a number of planes, as illustrated in Fig. 9b to 9d. Gross necking was typically absent, but there were cases with some necking. Specimens with shear-type fracture exhibited low values of R_A, and high values of the embrittlement index, indicating significant hydrogen embrittlement.

3.3.2 MS980 and MS1180

Fig. 10 shows typical cup and cone fracture for MS980 charged at -1.800 $V_{Ag/AgCl}$ and stressed at an applied stress rate of 0.064 MPa s^{-1}. MS980 displayed high ductility, as evidenced by the cup-and-cone fracture, extensive necking, the high value of R_A, and dimples at higher magnification as presented in Fig. 10b. Figs. 10c and 10d show that there were

shear bands in the necked region on the specimen surface. These shear bands were the result of strain localization at the surface of the steel in the necked region [43]. There were no cracks in the specimen surface.

The MS980 specimens tested, whilst charged at -1.200 $V_{Ag/AgCl}$ and -1.500 $V_{Ag/AgCl}$, showed similar cup and cone fractures, shear bands in the necked region, and no surface cracks.

Fig. 11 presents the fracture appearance of MS1180 charged at -1.800 $V_{Ag/AgCl}$, and stressed at an applied stress rate of 0.054 MPa s^{-1}. Fig. 11a presents the top view of the fracture, which was a typical cup and cone fracture, with typical dimple rupture as illustrated in Fig. 11b. There were, in addition, some regions of hydrogen cracking initiating from the surface. Fig. 11c presents the image from the short transverse side. This showed surface cracks concentrated in the neck area. These cracks were mostly horizontal, and were mostly oriented perpendicular to the tensile stress direction; although there were some cracks near the fracture lip, oriented at 45^{o} to the tensile direction. A comparison of Fig. 11a and Fig. 11d, indicates that the central area of the specimen tested whilst charged at -1.800 $V_{Ag/AgCl}$ was noticeably smaller than that in the uncharged specimen tested in air.

The MS1180 specimens tested whilst charged at -1.200 $V_{Ag/AgCl}$ and -1.500 $V_{Ag/AgCl}$ showed cup and cone fractures, high ductility, and no cracks associated with hydrogen on the specimen surface.

3.3.3 MS1300 and MS1500

Fig. 12 presents the shear type fracture for MS1300 and MS1500 charged at -1.800 $V_{Ag/AgCl}$, and tested at an applied stress rate of 0.080 MPa s^{-1}.

The MS1300 and MS1500 specimens tested, whilst charged at -1.200 $V_{Ag/AgCl}$ and -1.500 $V_{Ag/AgCl}$, showed similar shear type fractures, although there was some necking (i) for MS1300 specimens tested whilst charged at -1.200 $V_{Ag/AgCl}$ and -1.500 $V_{Ag/AgCl}$ and (ii) for MS1500 specimens tested whilst charged at -1.200 $V_{Ag/AgCl}$.

Fig. 12 indicates that the shear type fractures were similar for MS1300 and MS1500 charged at -1.800 $V_{Ag/AgCl}$, and tested at an applied stress rate of 0.080 MPa s^{-1}. Fig. 12a indicates that the fracture initiated at the locations designated as T at the specimen edges.

These areas exhibited mixed trangranular and intergranular cracking, as illustrated in Fig. 12d. The shear crack propagated mainly from the T region at the bottom left of Fig. 12a, as indicated in Fig. 12a by the arrows. Similarly, the arrows in Fig. 12b indicate the direction of the shear crack propagation. The S region possessed shear microvoid dimples. The dimples were large and deep at the centre, as illustrated in Fig. 12c, and became smaller and shallower near the fracture edges, as illustrated in Fig. 12e. The T regions were flat, and were oriented perpendicular to the tensile direction. Fig. 12d illustrates the mixed mode transgranular and intergranular fracture. The transgranular fractures were flat and quasi-brittle. The intergranular fracture was evidenced by the faceted fracture features, attributed to the prior-austenite grain boundaries. The T regions often had an approximately semicircular or semielliptical shape, as traced on the surface, in Figs. 12a and 12b. The dimples in the S areas indicated localised plasticity and ductile tearing, whilst the features in the T areas indicated brittle behaviour.

For MS1300, the shear fracture appeared blocky, and the two areas of fracture were easily identifiable. The direction of crack propagation is indicated by the arrows in Fig. 12a. The crack initiated at a corner or a sharp edge at a T region, in the lower left corner. The crack propagation region, a majority of which was the S region, accounted for more than 80% of the fracture area. The shear crack propagated towards the right, and met the two T regions on the right hand side of the specimen. These two T regions had initiated in a manner similar to the T regions on the left hand side of the specimen.

For MS1500, shown in Fig. 12b, there was a crack initiation region in the lower left corner of the fracture surface that (i) possessed small, shallow shear dimples, and (ii) displayed some secondary cracks that were oriented parallel to the direction of the tensile stress. The region of main crack propagation showed shear dimples, with the dimples becoming shallower as the crack approached the other specimen edge. The fracture surface also had a T region, which originated from the opposite edge, and initiated shear cracking that met the advancing shear fracture.

Fig. 13 presents (i) the side view for MS1300 and MS1500 specimens, and (ii) details of the horizontal surface cracks present near the fracture region. These images indicate the presence of intense localized plastic deformation at the edges that coincided with the surface crack initiations. The volume associated with this deformation was much smaller than that

associated with a typical neck. The surface cracks in the MS1500 specimen were similar in length to those of the MS1300 specimen, but were more numerous, and had opened more.

3.4 Fractography at the lowest applied stress rates

Fig. 14 compares the fracture appearance of the four grades of MS-AHSS, charged at -1.800 $V_{Ag/AgCl}$, and tested at the lowest applied stress rates. Figs. 15 and 16 present additional details of the top view of the fracture surfaces, whilst Fig. 17 compares the fractures from the transverse view. These fractures were shear-type fractures. Fig. 15a illustrates typical shear dimples, which occurred throughout the regions designated S. Fig. 15b illustrates typical mixed transgranular and intergranular fracture, which occurred in the regions designated as T. The shear dimple characteristics varied with location, becoming finer and shallower near the edges, which is illustrated in Fig. 15d. Fig. 15c illustrates a new mixed fracture region, designated as M, which exhibited a combination of ductile and brittle behaviour. These regions had large shear dimples interspersed with flat brittle zones, and sometimes exhibited fisheyes.

Fig. 14 shows that, for MS980, tested at the lowest applied stress rate of 0.0064 MPa s^{-1} and charged at -1.800 $V_{Ag/AgCl}$, the fracture surface was comprised of shear dimples, accompanied with some necking as confirmed by Fig. 17a.

Fig. 14 shows that, the fractures of MS1180, MS1300 and MS1500, at the slowest stress rates and charged at -1.800 $V_{Ag/AgCl}$, were similar. There was no necking. There were indications of brittle behaviour, such as the T regions. There were surface cracks near the fracture. There were M regions, which were not present for the specimens tested as the intermediate stress rate. For MS1300 and MS1500, the shear-type fracture was sharper, which refers to the fracture breaking cleanly in a single shear plane.

Fisheyes were present on the fracture surfaces of MS1300 and MS1500 specimens. Fig. 16 illustrates typical fisheyes. Each fisheye was a region of brittle fracture that initiated, and grew from a macroscopic defect [44], such as a void, inclusion, carbide, or a small martensite grain. The defect was typically located at the pupil or centre of the fisheye. Each brittle crack appeared to have initiated at the central defect, and to have grown radially in an approximately circular manner to sizes that ranged from 10 to 50 μm. There was typically dimple rupture surrounding the fisheye. There was, in the centre of most of the fisheyes,

either a void, as illustrated in Fig. 16a, 16b and 16d, or a fractured particle, as illustrated in Fig. 16c. Fig. 16d illustrates a particle with a central void. Back-scattered electron imaging indicated that this particle was not an inclusion. The geometric holes were the space left by an uprooted phase, since typical voids assume a round shape. Judging from its characteristics, the phase was most likely martensite.

4. DISCUSSION

4.1 Metallurgy

The microstructures indicated the major micro-constituent was martensite as expected for these grades of AHSS. The type of martensite was most probably the lath type, which is expected for steels with carbon content less than 0.6% [45]. Martensite is produced by rapid cooling of high-temperature austenite [46]. Martensite is the strongest of the ferrous microstructures, with low ductility. In addition, there was a minor amount of ferrite. Ferrite, or alpha-iron (α-Fe), is a soft ferrous microstructure, possessing the body-centered cubic (BCC) structure. The presence of ferrite would decrease the overall strength, but would increase ductility and toughness.

The presence of both ferrite and martensite in the microstructure of each steel reveals the thermal history of the steels. A purely martensitic structure is expected when hot austenite is quenched at, or above, the critical cooling rate [47]. For low carbon steels, the continuous cooling transformation (CCT) curves predict the presence of ferrite and martensite for quenching at a cooling rate lower than the critical rate [48]. Alternatively, the steel may have been quenched from an inter-critical temperature, at which temperature the microstructure consisted of ferrite plus austenite, with the quench transforming the austenite to martensite, but having no influence on the ferrite. Since strength is directly proportional to the amount of martensite, it would seem that the inter-critical annealing temperature was used to control to the proportions of martensite in the final microstructure. Stronger steels can be produced using a higher inter-critical annealing temperature where there is a greater amount of austenite, so that subsequent quenching produces more martensite.

The etched features in the martensite, in Fig. 4b, suggested auto-tempering. Auto-tempering occurs when martensite is tempered by the hot core of the steel sheet during cooling. Auto-tempering is beneficial as it softens the martensite, and reduces brittleness.

Matsuda et al. [49] observed greater etching of martensite in steels with greater auto-tempering. Auto-tempering is likely in steels with a high martensite-start temperature [50], which is expected for these MS-AHSS steels, because of their low alloy composition.

The appreciable strength of these steels (see Table 1) may be attributed to the amount and nature of the martensite in their microstructures. Martensite hardness is dependent on carbon content. Thus the higher strengths of MS1300 and MS1500 may be attributed to the higher carbon concentrations and high fraction martensite. Table 2 indicates that, to a first approximation, the steel strength was proportional to the relative amount of martensite. Furthermore, the strength of the MS-AHSS may have been slightly reduced by auto-tempering, which was confirmed to have occurred in all the samples.

There is a possibility that there might be some retained austenite. Unfortunately, the etchant does not allow retained austenite to be distinguished from martensite [39], and these two phases are indistinguishable in the micrographs. The presence of retained austenite is unwanted in a martensitic matrix. Retained austenite is unstable at room temperature, and transforms to other microstructures such as martensite, bainite and pearlite [47]. This transformation involves volume changes that produce residual tensile stresses, and this initiates easy fracture, especially in the ductility-poor martensite.

Table 3 and Fig. 6 indicated that the influence of hydrogen increased in the order of MS980, MS1180, MS1300 and MS1500. The steels in this order have (i) increasing carbon contents which would be expected to produce stronger martensite, (ii) increasing steel strength (see Table 1), (iii) increasing volume fraction of martensite in the microstructure (see Table 2) and (iv) decreasing volume fraction of ferrite in the microstructure (see Table 2). The increasing steel strength is consistent with a rule of mixtures relating to the strength of ferrite and martensite, with martensite strength increasing slightly. The working hypothesis is thus that increased hydrogen influence is determined largely by the microstructure and related somehow to hydrogen trapping. It is intended to test this hypothesis as a later part of this research project in which there will be an investigation of hydrogen trapping using permeability experiments and thermal desorption spectroscopy.

4.2 Mechanical properties in air

The values of yield and tensile strengths determined using LIST for the MS-AHSS presented in Table 3 were comparable with the values in Table 1 supplied by the steel supplier, and based on standard tensile tests. This confirms that the testing conditions in the LISTs in air were comparable with those of conventional tensile tests. In particular, in the LISTs, yielding could be correctly detected, and thus the yield stress could be correctly measured. The LIST is different to a tensile test in that the LIST is load controlled so that the onset of necking occurs at the ultimate tensile stress. In the LIST, there is plastic instability at the ultimate tensile stress leading to rapid fracture of the sample. In contrast, a conventional tensile test is strain controlled, and the sample is allowed to elongate after the ultimate tensile stress until fracture. Nevertheless, the fracture stress measured using the LIST corresponds to the ultimate tensile stress as measured in the tensile test. This confirms that the LIST has been accurately calibrated, and could accurately measure the yield stress, and the ultimate tensile stress.

Table 3 indicates that there might have been a slight increase in strength with increasing applied stress rate. If there were a slight increase, rather than the measurements being within experimental scatter, this slight increase would be in agreement with literature as tensile strength are known to increase with increasing applied stress rate [51]. This is attributed to a faster rate of dislocation creation, leading to greater dislocation entanglement and stronger strain hardening effects. Nevertheless, the difference was small, and may be considered to be within experimental scatter.

Table 3 indicated that the values of R_A were substantial in all the steels, in the uncharged condition. The substantial values of R_A indicated ductile behaviour, consistent with the appearance of each specimen after the LIST, showing a necked region, and a cup-and-cone fracture. The criss-cross bands on the specimen surface in the neck regions were identified as shear bands, as they were oriented at 45° to the tensile direction, which coincided with the direction of maximum shear stress. Shear bands are manifestations of strain localization in the dislocation-driven plastic deformation of metals [43]. The bands were formed in the neck region, especially near the fracture, where there was intense plastic deformation.

4.3 Mechanical properties at the intermediate stress rate

4.3.1. MS980 and MS1180

Table 3 indicates that, at the intermediate applied stress rates, the values of σ_{TH}, σ_F and R_A were similar to the corresponding values measured in air, for all values of cathodic charging potential. The fact that there was a small difference between the values in air, and at all levels of hydrogen charging, indicates that there was little influence of hydrogen on the strengths of MS980 and MS1180. The small influence of hydrogen was consistent with the low values of hydrogen embrittlement susceptibility, S_H, in Fig. 6b, and by the low values of the embrittlement index, I, in Fig. 6c. Table 3 and Figs. 6a-c shows that there was some decrease in the values of threshold stress and of R_A for MS1180 in the test with a cathodic charging potential of -1.800 $V_{Ag/AgCl}$, indicating some influence of hydrogen. Fractographic images in Fig. 10 and 11 gave similar conclusions. Thus, these results indicated that (i) there was little influence of hydrogen up to the yield stress, (ii) the yield stress in the presence of hydrogen had decreased, attributed to solid solution softening, (iii) there was no sub-critical crack growth due to hydrogen, and (iv) that the influence of hydrogen in the MS1180 specimen tested at -1.800 $V_{Ag/AgCl}$, was associated with the final ductile fracture process when the specimen had become mechanically unstable.

4.3.2. MS1300 and MS1500

Table 3 and Fig. 6a indicate that, for MS1300 and MS1500 at the intermediate applied stress rates, hydrogen decreased the mechanical properties, both σ_{TH} and R_A; leading to substantial values of the hydrogen susceptibility index, S_H, as indicated in Fig. 6b, and substantial values of the embrittlement index, I, as indicated in Fig. 6d. Fracture images, as documented in Figs. 12 and 13, confirm the loss of ductility for these steels. The images in Figs 12 and 13 however were not consistent with the majority of the fracture being caused by subcritical crack growth starting at the threshold stress. Rather, these images were consistent with the fracture occurring at the ultimate tensile stress when the specimen had become mechanically unstable. The Linearly Increasing Stress Test (LIST) is load controlled, and the specimen becomes mechanically unstable at the maximum stress, and fracture ensues.

The decrease in σ_{TH} is thus interpreted as indicating a substantial decrease of the yield stress by hydrogen. The influence on σ_F was also small, of similar magnitude to the decrease

in the yield stress, and is interpreted in a similar manner, i.e. the influence of hydrogen in facilitating plastic flow.

The susceptibility of MS1300 and MS1500 to HE is relatable to their high strength. It is well known that HE susceptibility increases with increasing strength [16, 52]. For example, Lynch [16] indicated that tempered martensitic steels with strengths greater than 900 MPa are susceptible to hydrogen embrittlement. The presence of the martensite phase is also an aggravating factor [53, 54].

While it is widely accepted that high-strength steels are susceptible to HE, using strength alone as guide for predicting HE may not be prudent. Loidl et al [21] compared several types of AHSS and found that, while MS-AHSS have the highest strength, other grades such as TRIP and DP were more susceptible to HE. Lovicu et al [18] observed similar tendencies for AHSS, and noted that these steels have different hydrogen uptakes depending on factors such as chemical composition, process history, residual stress, and microstructure. The differences in hydrogen uptake can lead to a range of HE susceptibilities. It is important, when considering the influences of microstructure of these MS-AHSS, to consider the influences of the ferrite and retained austenite that are in these steels. For example, Begic Hadzipasic et al [54] cited lower HE vulnerability in TRIP-AHSS due to the presence of retained austenite. The effect of auto-tempering of the martensite should also be considered. Bates and Loginow [55] observed a decrease in HE susceptibility when martensitic steels were tempered. What is clear is that new models for accurate HE prediction in AHSS are needed since rules applicable to conventional steels may not be relevant.

Hydrogen had only a small influence on the yield and fracture strength of these MS-AHSS. These observations are similar to recent results of Liu et al [37] studying medium strength steels using the LIST, and Loidl et [21] studying different AHSS using slow strain rate tests (SSRTs). Both studies concluded that strength parameters were not influenced by the presence of hydrogen; although the latter was responsible for altering ductility at fracture. In contrast, Lovicu et al [18] investigated MS-AHSS using SSRT and reported a significant decrease in yield and tensile strength with increasing hydrogen content. Similarly, the stronger grades of AHSS were more sensitive to hydrogen.

4.3.3. Charging Potential

Table 3, Fig. 6b and Fig. 6c indicate that increasing charging potential increased the hydrogen influence for MS1300 and MS1500 at intermediate rates. Atrens and co-workers [56, 57] considered the relation between hydrogen fugacity, f, and cathodic electrochemical charging overpotential, η. For a low interstitial steel, Liu et al. [57] found that hydrogen fugacity could be related to η as follows:

$$f = 10.9 \exp\left(-\frac{\eta F}{16.47RT}\right) \quad (5)$$

where F is the Faraday constant, R the gas constant, and T is the temperature in K. The corresponding hydrogen concentration inside the steel, C, is given by Sievert's Law [58]:

$$C = K_s\sqrt{f} \quad (6)$$

where K_s is the solubility constant.

These equations indicate that increasing the charging over-potential increases the hydrogen fugacity, and, consequently, the hydrogen concentration in the steel. This increase in hydrogen concentration increases the vulnerability of the steel to HE. Similar conclusions were attained in various works [16, 18, 38, 59, 60]. Marchetti et al [60] also suggested the possibility of an increase in the hydrogen diffusion coefficient at an higher hydrogen activity, due to the fact that more hydrogen traps were already filled.

For MS1300, the hydrogen embrittlement index became large after charging at -1.500 $V_{Ag/AgCl}$. Since the charging potential can be related directly to the hydrogen concentration, this result is consistent with the concept of a threshold hydrogen concentration [16, 18, 61]. This is the minimum hydrogen content that causes a significant reduction in the ductility, or threshold stress, and causes HE. For MS1500, it is likely that the threshold concentration was attained at the charging potential of -1.200 $V_{Ag/AgCl}$. Furthermore, it is also conceivable that though MS980 and MS1180 did not display embrittlement up to -1.800 $V_{Ag/AgCl}$ at intermediate stress rates, a higher charging potential may cause the onset of HE.

4.4 Mechanical properties at lowest stress rate

Table 3, Fig. 6b and Fig. 6c indicate that the combination of lowest applied stress rate and hydrogen charging at the most negative applied potential caused (i) a reduction in σ_{TH}, σ_F and R_A, (ii) an increase in the hydrogen susceptibility index, S_H, and (iii) and increase in the

hydrogen embrittlement index *I*. This influence was greater in the two strongest grades, i.e. MS1300 and MS1500. For MS980, the increase in *I* was modest, and occurred only at -1.800 $V_{Ag/AgCl}$. For MS1180, the embrittlement index, *I*, indicated considerable embrittlement at -1.500 and -1.800 $V_{Ag/AgCl}$. The corresponding fractographs (Fig. 14) provide support. There was necking and macro-ductility in MS980, whilst in MS1180, MS1300 and MS1500 there were macroscopically brittle shear fractures, accompanied by little, if any, plastic deformation. Nevertheless, the fractographs of Fig. 14 were similar to those in Fig. 12 and 13, and were consistent with that interpretation: that the majority of the fracture occurred at the ultimate tensile stress when the specimen had become mechanically unstable. This would imply also that the presence of hydrogen in these steels had decreased the yield stress.

The major difference between the tests with the low and the intermediate applied stress rates was that the specimens were exposed to much longer periods of hydrogen charging. For example the test required 6 hours for the MS1300-1.8-30 specimen at the applied stress rate of 0.080 MPa s^{-1}, after the initial 24 hours charging. This means a total hydrogen exposure time of 30 hours for this specimen. However, for MS1300-1.8-3 which was tested at the applied stress rate of 0.0080 MPa s^{-1}, the test finished after 44 hours; i.e. a total of 68 hours charging time. There was an obvious increase in charging times.

To eliminate the variable charging time, a test was carried at the intermediate stress rate but with the total charging times equal to that with the low applied stress rate (i.e. 68 hour). The result is presented as MS1300-1.8-30-L. The LIST data obtained for MS1300-1.8-30-L were the same as those of MS1300-1.8-30 within experimental error. This result led to two conclusions. Firstly, the application of a low stress rate during charging caused the observed difference in mechanical response of the steels. Secondly, after the initial 24 hours of charging, embrittlement susceptibility was independent of charging time. If HE is correlated to the total amount of hydrogen present in the specimen, then the results imply that hydrogen content had indeed reached equilibrium, and became relatively constant at this time. The behaviour was consistent with permeation studies that observed a steady hydrogen concentration gradient occurring in conventional steels after a charging interval of 24 to 48 hours [57, 62, 63]. A constant hydrogen concentration throughout the specimen after 24 h charging was also consistent with the fact that permeation transients took only several hours in comparable steels of comparable thickness [64].

The stress rate dependence of HE susceptibility in the current study agreed with known the strain rate dependence of HE in steels [65-68]. These studies indicate that HE is favoured by slow deformation rates, and that HE becomes apparent only below a critical rate of stressing, consistent with Fig. 6b. Consequently, impact testing is not useful in studying HE [67]. Some studies even suggest that maximum susceptibility to HE is revealed when static loads are used, and early HE tests were indeed based on using static loads [59, 69].

HE necessitates time for hydrogen adsorption, and diffusion [59]. Additionally, hydrogen diffusivity in martensitic steels is inherently low due to the high defect density [63], therefore hydrogen assimilation and diffusion is indeed more favourable at slower stress or strain rates. However, considering the results of permeation studies done on steel [57] coupled with the length of pre-charging times, it is reasonable to assume that hydrogen concentration in the specimen was already uniform when the stress was applied. This would mean that any hydrogen diffusion enhancement occurring in the samples could only result from stress interactions. Hashimoto and Latanision [68] proposed that the strong strain-rate dependence of HE is due to dynamic trapping of hydrogen by moving dislocations in face centred cubic alloys. They explained that the hydrogen-carrying dislocations were created during plastic deformation, and slow straining allows dislocations to reach farther within the alloy. This trapped hydrogen interacts with a greater mass of the alloy, and is responsible for causing embrittlement. Alternatively, the important aspect could be the local diffusion of hydrogen in the triaxial stress field at the crack tip, as shown by Gerberich [70].

In contrast, Liu et al [38] did not observe this stress rate dependence using LIST on medium-carbon medium-strength martensitic steel. Momotani et al [71] also reported strain-rate independence of HE susceptibility of hydrogen-charged low carbon martensitic steels. Thus, an explanation of the stress rate dependence of HE susceptibility of these MS-AHSS steel appears to be more complex, and may require a comprehensive consideration of factors such as microstructure, fabrication history, etc.

Few studies deal with the influence of the applied stress rate on HE, such as the present research with the LIST, since the more common approach is to control the extension rate using CERT [72], and to conduct experiments at a moderate extension rate, equivalent to a strain rate of 10^{-6} s^{-1}. However, constitutive equations for stress and strain have established a direct correspondence between the two, in the initial elastic part of the tests [51], and no conflict between the use of either concept is perceptible. Moreover, Winzer et al [31] showed

that both approaches, stress-control via LIST and strain-control via SSRT, yielded comparable data, and may be used to assess HE with competency.

4.5. Fractography

4.5.1 Ductile Fracture

The fractography indicated that there was little hydrogen influence for specimens exhibiting cup-and-cone fracture, see Figs 7, 8, 10 and 11. These cup-and-cone fractures were exhibited by (i) the uncharged steels, (ii) MS980 charged at all three charging potentials, and (iii) MS1180 charged at -1.200 $V_{Ag/AgCl}$ and -1.500 $V_{Ag/AgCl}$, at the intermediate applied stress rate. A cup-and-cone fracture, coupled with substantial necking, indicated ductile behaviour. The dimples on the fracture surface indicated microvoid coalescence (MVC) [73]. The microvoid coalescence involved four main stages: a) void nucleation, b) void growth, c) void coalescence and crack extension, and d) separation of the remaining ligament via shear. The two distinct areas on the ductile fracture surfaces, in Figs 7 and 8, related to the stages of MVC. The central area was the region of void initiation, growth, and crack growth by micro-void coalescence. The spherical shape of the dimples indicated that the applied tensile force caused tearing in this section. To a first approximation, the depth of the dimples could reflect the ductility of the steel. Deeper dimples relate to higher ductility. The final stage of fracture was outside the central region, at a 45^{o} slope with respect to the tensile direction. This orientation, and the elongated and parabolic dimples, indicated the action of shear stress, which caused the final rupture. Furthermore, the shear bands also provided evidence of substantial plastic strain.

The fractography of MS980, charged at all three charging potentials, indicated essentially no influence of hydrogen, at the intermediate applied stress rate.

In contrast, for MS1180, the fractography indicated ductile fracture, with some influence of hydrogen. The hydrogen-charged specimens had a central area smaller than that of the uncharged specimens, which indicated a higher sensitivity to the presence of a crack. A small central area means that the ductile micro-void coalescence crack initiated, and grew to a smaller size, before the presence of this central crack initiated the final shear fracture at the edges of the specimen. Hydrogen has been found to reduce the shear modulus [27], and this may have induced such increased crack sensitivity in MS1180. Alternatively, it is possible

that this greater sensitivity could have been caused by the propensity for hydrogen to induce localised plasticity by the AIDE and HELP mechanisms. Another indication of the influence of hydrogen was the presence of cracks on the specimen surface, concentrated in the neck area. A discussion on these surface cracks is presented in a succeeding section.

4.5.2. Shear Fracture

In contrast, the shear fractures, such as those for MS1300 and MS1500 with hydrogen charging at -1.800 $V_{Ag/AgCl}$, were related to some hydrogen influence as evidenced by the reduced values yield stress, tensile stress, and reduction in area being lower than the corresponding specimens tested in air, see Table 3 and Figs. 6, 9, 12-17. Thus, analyses of the hydrogen-influenced failures indicated that hydrogen promoted a shift to shear fracture. This shear fracture was microscopically ductile as illustrated in Figs. 12a and 15a, but was macroscopically brittle, as indicated by the absence of necking, and the loss of macroscopic ductility.

Crack initiation of shear fractures occurred at the surface, from a T region in Fig. 12a, and shear regions at sharp corners, as indicated in Figs. 12b, and Figs. 13a-d; whereas the crack initiated in the centre of the fracture in the ductile cup and cone fracture. This is consistent with the fact that the hydrogen concentration was highest at the surfaces for electrolytically-charged steels [63], because the hydrogen entered the steel through the specimen surface. Therefore, it is logical that the highest influence of hydrogen was at the external surfaces. Moreover, the stress intensity factor for a surface defect is double that of a similar internal defect [51].

The presence of intense, and highly-localized, plastic deformation is consistent with two hydrogen embrittlement mechanisms: the hydrogen-enhanced local plasticity (HELP) and the adsorption-induced dislocation emission (AIDE) mechanism. The HELP mechanism proposes that solute hydrogen augments the plastic response, and severely localises this plasticity. The severely localised plastic deformation reduces the possibility of necking, and the measured macroscopic ductility becomes insignificant. In contrast, the AIDE mechanism, proposes crack initiation and growth via dislocation emission due to hydrogen adsorption at the surface, or at the advancing crack tip. In the AIDE mechanism, the emphasis is on crack nucleation and growth as facilitated by hydrogen adsorption at the surface, whilst HELP

focuses on the hydrogen dissolved in the metal. Both mechanisms expect the crack initiation site to show localized plasticity. Similarly, both mechanisms can explain the observed ductile shear dimpling in the shear crack propagation stage. This indicates that the fractographic evidence is consistent with both the HELP the AIDE mechanisms for the shear fractures, and can exclude the HEDE mechanism, but the fractography alone cannot distinguish between the two mechanisms of HELP and AIDE.

The AIDE mechanism may be indicated by (i) the fact that fast fracture occurred at the plastic instability condition coincident with the ultimate tensile stress (UTS), and (ii) hydrogen caused a small decrease of both the LIST flow stress and UTS. The fact that hydrogen was electrolytically charged during LIST, and that hydrogen was introduced primarily via surface adsorption may also favour AIDE. On the other hand, the 24-hour pre-charging would have ensured the presence of enough solute hydrogen throughout the specimen, which is necessary to activate the HELP mechanism. The combination of the AIDE and HELP mechanism may have caused the shear fractures. This combination is possible depending on the type of material, physical properties and other variables [74]. Crack initiation, mostly at the edge, may have started with hydrogen adsorption and dislocation emission by AIDE. Dynamic unstable fracture propagation with the subsequent microvoid nucleation ahead of the advancing fracture front may have been aided by localized plasticity via the HELP mechanism. Another way by which the HELP mechanism enhances AIDE, is when HELP causes the emitted dislocations to move away from the crack tip more readily, which lessens the back-stress on subsequent dislocation emissions and improves crack propagation [16].

Shear-induced fracture of AHSS in the absence of hydrogen influence has been reported previously [75-77]. Press shops gave an early account of the so-called stretch bending fracture, which occurred during the stamping of AHSS sheets. Shear failure occurred at strains lower than the formability limit, and greatly limited allowable part geometries. Wagoner et al [78, 79] provided evidence that plastic strain localization, rather than brittle crack propagation, caused shear fracture during stretch bending. This statement is consistent with observations made in the current study, where dimpling was present in the majority of the fracture surface area. It is apparent that a common aspect of these two (i.e. the stretch bending and the hydrogen–charged) shear fractures is strain localization. It is thus conceivable that the hydrogen-induced shear fracture in MS-AHSS were initiated by the strain localizations created by hydrogen via the AIDE and HELP mechanism. Surprisingly,

Huang et al [76] found that MS-AHSS, though being less ductile, showed higher resistance to shear fracture than the dual-phase (DP) AHSS.

Whilst MS1300 and MS1500 both showed strain localization, the two differed in the features at the initiation region of the major crack, see Fig. 12. MS1300 possessed an initiation region with a more brittle appearance, as initiation coincided with the T region, which consisted of the mix of intergranular and transgranular fracture. The orientation of crack initiation was perpendicular to the tensile direction, and suggested sensitivity to the action of the tensile stress. In contrast, the crack initiation was a shear type fracture for the MS1500 specimen, which was accompanied by extensive dimples. The fracture initiation for the MS1500 specimen may be explained by HELP or AIDE mechanism. In contrast, initiation for MS1300 is attributed to a HEDE mechanism, because there was little sign of ductility in the mixed intergranular and transgranular T region. Intergranular fracture occurs when hydrogen segregates at or near grain boundaries and there is sufficient hydrogen to allow fracture along grain boundary paths [16, 26]. Transgranular fracture occurs for cases when the same mechanism happens inside the grain.

4.5.3 Surface Cracks

Another manifestation of the influence hydrogen was the occurrence of cracks in the surface of the specimens. All these cracks occurred close to the final fracture. For a ductile fracture, such as that illustrated in Fig. 11c, these cracks occurred exclusively in the neck region. For the brittle shear fractures, most surface cracks were concentrated near the final fracture; although, there were several cracks also at some distance from the fracture. Such surface cracks are associated with the final fracture process when the specimen has become mechanically unstable. That means that the hydrogen assisted cracks competed with ductile fracture processes.

The occurrence of surface cracks in areas of localized plastic deformation is consistent with the HELP and AIDE mechanisms. The high local stress in the neck can cause an increase in the concentration of hydrogen in this region due to (i) the decrease in the chemical potential of the solute hydrogen, (ii) an increase of ease of hydrogen ingress as plastic deformation breaks surface barriers to hydrogen entry, and (iii) and an increase in hydrogen traps (particularly dislocations and vacancies). However, it must be remembered that necking occurs only during final fracture in a load-controlled test such as a LIST, and there is little time for changes in hydrogen concentration. Multiple hydrogen-assisted

cracking events can occur in the neck as localized strains, created by the HELP and/or the AIDE mechanism, exceed the strain limits. Alternatively, the local high hydrogen concentration in the plastically deforming neck region can trigger brittle intergranular and transgranular cracks via HEDE, which compete with other fracture events.

For the shear fractures, it is conceivable that the surface cracks, near the final fracture, were formed by a ductile HELP or AIDE mechanism as described above.

The occurrence of surface cracks outside of the plastically-deformed areas may indicate hydrogen damage. The high hydrogen fugacity during cathodic charging is known to cause hydrogen damage [26], although there were no signs of such damage in these specimens.

4.5.4 Fracture at the lowest stress rates

At the lowest applied stress rates, see Table 3, Fig. 6 and Figs. 14 to 17, the hydrogen influence increased with the strength of the steel grade. For MS980, there was (i) little hydrogen influence and cup and cone fractures at the hydrogen charging potentials of -1.200 $V_{Ag/AgCl}$ and -1.500 $V_{Ag/AgCl}$; and (ii) some some hydrogen susceptibility at -1.800 $V_{Ag/AgCl}$, as evidenced by the shear type fracture. For MS1180, there was (i) no hydrogen influence at -1.200 $V_{Ag/AgCl}$, but (ii) shear type fractures and hydrogen influence at -1.500 $V_{Ag/AgCl}$ and -1.800 $V_{Ag/AgCl}$. MS1300 and MS1500 already displayed significant hydrogen influence at the intermediate stress rate at all charging conditions. Therefore, at the lowest stress rate of 0.008 MPa s^{-1}, specimens of these steels were tested only at the most severe charging potential of -1.800 $V_{Ag/AgCl}$, which indicated (i) increased hydrogen influence, (ii) shear type fractures, and (iii) most severe hydrogen influence for MS1500.

Fig. 14 indicates that there was an obvious reduction in the area of the S region, and an increase in the area of the T and M regions with increasing steel strength for the steels tested at the most severe charging potential of -1.800 $V_{Ag/AgCl}$. This implies a shift from the macroscopically brittle shear type fracture to a more brittle type behaviour. The shear fractures also occurred in a single shear plane. At the faster applied stress rate, some of the shear fracture propagated along different planes. Multi-planar crack growth requires deflecting the advancing fracture tip to assume different directions. Such a process entails dissipation of more energy, and increases somewhat the fracture toughness. Conversely,

fracture limited to a single shear plane requires less energy, and the behaviour is more brittle. The increased hydrogen influence in the MS-AHSS at the lowest applied stress rates was thus indicated by (i) the decreased S regions and increased T and M regions, and (ii) the more planar shear fractures. The increased hydrogen influence at the lowest applied stress rates was consistent with the known strain-rate sensitivity of HE [59, 66]. The shear fractures are also attributed to the HELP/AIDE mechanisms as discussed earlier, and the brittle intergranular-transgranular fractures were attributed to HEDE.

Fisheyes were present on the fracture surface of MS1300 and MS1500 steel only at the lowest applied stress rate with hydrogen charging. Fisheyes are manifestations of hydrogen embrittlement [80]. The fact fisheyes occurred only in the two strongest steels tested at the slow stress rate led to the following conclusions. Firstly, fisheye formation was stress-rate dependent, and occurred preferentially at low applied stress rates. This was confirmed in the experiment (with specimen MS1300-H1.8-30-L) conducted to eliminate the variable of charging time, and thus isolate the effect of stress rate. This specimen did not exhibit any fisheyes. Secondly, fisheye formation was dependent on the type of MS-AHSS, and occurred preferentially in the higher strength grades. To identify the main factor in the steel, e.g. microstructure, carbon content, residual stress, etc. that caused the fisheyes is difficult. What was apparent was that martensite was involved in fisheye formation, as the crack initiator.

Fisheyes are typically associated with the internal hydrogen content, i.e. the amount of hydrogen present in the material. This is because fisheyes are usually found away from the surface of the steel. Similarly in this research, the majority of the fisheyes occurred near the centre of the specimen. Fisheyes are thought to be caused by a combination of two factors: (i) hydrogen accumulation at an imperfection (storage effect), and (ii) plastic deformation [44]. The formation of a fisheye begins with the accumulation of hydrogen at a volume defects (e.g. a voids or an inclusion at the boundary) [81]. Since the MS-AHSS contained both martensite and ferrite, it is suspected that the martensite-ferrite phase boundary was the hydrogen storage site. The physical and mechanical incompatibility between these two phases possibly created the discontinuity at which hydrogen accumulated. Plastic deformation is thought to increase the hydrogen uptake due to the ability of dislocations to transport hydrogen [68]. However, steady hydrogen accumulation requires time, both for hydrogen-bearing dislocations to reach the storage site, and for ample hydrogen diffusion to take place. Both of these processes favour slow strain or stress rates. At high deformation rates,

dislocations are created rapidly but lead to more entanglement during slip [67]. This becomes counter-productive to hydrogen accumulation as it halts hydrogen-bearing dislocations from reaching the intended site. In addition, plastic deformation increases hydrogen uptake because plastic deformation introduces hydrogen traps (particularly vacancies and dislocations).

Fig. 16 illustrates typical fisheyes. Each fisheye contained a defect typically located at the pupil or centre of the fisheye. Each brittle crack initiated at the central defect, and grew radially in an approximately circular manner to sizes that ranged from 10 to 50 μm. There was typically dimple rupture surrounding the fisheye. The fact that the brittle fracture of the fisheye was typically surrounded by dimple rupture indicates that (i) fisheyes occurred during the final fracture process, and (ii) the brittle fracture process of fisheye formation was competing with concurrent microscopically-ductile shear type fracture.

4.6. Hydrogen influence

A key observation was that there was necking associated with some of the shear fractures associated with hydrogen. For example, Table 3 records necking for shear fractures at the intermediate applied stress rate for (i) MS1300 specimens tested whilst charged at -1.200 $V_{Ag/AgCl}$ and -1.500 $V_{Ag/AgCl}$ and (ii) MS1500 specimens tested whilst charged at -1.200 $V_{Ag/AgCl}$. Figs. 14a and 17a shows necking of the shear fracture for MS980, tested at the lowest applied stress rate of 0.0064 MPa s^{-1} and charged at -1.800 $V_{Ag/AgCl}$.

In LISTs, necking occurs only at the ultimate tensile strength when the specimen has become mechanically unstable (as in all load controlled tensile tests). These shear fractures with necking are essentially the same as the shear fractures in Figs. 12, 13 and 14b-d, and associated with essentially no necking and low macroscopic ductility. This implied that all the shear fractures occurred at the fracture stress and there was no sub-critical crack growth. This is consistent with there being only minor features on the fracture surfaces that could be interpreted as sub-critical crack growth, such as the T region in Fig. 12.

To check this conclusion that there was no sub-critical crack growth in the hydrogen charged specimens, a LIST was carried out using MS1300 at -1.800 $V_{Ag/AgCl}$ after 1 day hydrogen pre-charging, at an applied stress rate of 0.080 MPA s^{-1}, until the stress reached 80% of the expected fracture stress (i.e. to a stress well above the threshold stress).

Examination of the specimen, using optical and scanning electron microscopy, did indicate the complete absence of any sub-critical cracks.

Thus, the apparent threshold in the hydrogen charging environments is identified as a yield stress rather than a threshold stress for the initiation of subcritical cracking due to the presence of hydrogen. Fig. 6a indicates that the normalised yield stress for each steel decreased with increasing amounts of hydrogen in the specimen, decreased with steel strength, and decreased with decreased applied strain rate. This decrease in yield stress with hydrogen is attributed to solid solution softening by hydrogen.

Table 3 indicates that there were similar influences of hydrogen on the fracture stress. These decreases in the fracture stress, and the concomitant changes in fracture mode with hydrogen, are thus attributed to a dynamic interaction of hydrogen with the dislocation substructure, by a process that must be somewhat similar to the HELP mechanism for sub-critical crack growth influenced by hydrogen [25,70]. It is proposed that the dynamic interaction of hydrogen facilitating dislocation movement, as evidenced by the decreased yield strength, caused the transition of fracture from cup and cone to shear fracture in the presence of hydrogen.

5. CONCLUSIONS

The paper presents a LIST study of the influence of hydrogen on the mechanical and fracture properties of four commercial grades of MS-AHSS, with the hydrogen introduced by cathodic charging.

1. The hydrogen influence increased with steel strength, increasingly-negative charging potential and decreasing applied stress rate.
2. Increased hydrogen influence was manifest in the decreased yield stress, in reduced macroscopic ductility, and by the change from ductile cup-and-cone fracture to macroscopically brittle shear fracture.
3. The decrease in yield stress is attributed to solid solution softening by hydrogen.
4. The fractography was not consistent with the majority of the hydrogen-assisted fractures being caused by subcritical crack growth starting at the threshold stress. Rather, the fractography was consistent with the hydrogen influenced fracture occurring at the ultimate tensile stress when the specimen had become mechanically unstable.

5. The decreases in the fracture stress, and the concomitant changes in fracture mode with hydrogen, are attributed to a dynamic interaction of hydrogen with the dislocation substructure, by a process that must be somewhat similar to the HELP mechanism for sub-critical crack growth influenced by hydrogen.

ACKNOWLEDGEMENTS

This research is supported by the Baosteel-Australia Joint Research & Development Centre (BAJC) Grant, BA13037, with linkage to Baoshan Iron and Steel Co., Ltd of China.

The authors also acknowledge the facilities, and the scientific and technical assistance, of the Australian Microscopy & Microanalysis Research Facility at the Centre for Microscopy and Microanalysis, The University of Queensland.

References

[1] WorldAutoSteel. Advanced High-Strength Steels Application Guidelines V5.0. Published May 5, 2014. Available from http://www.worldautosteel.org. Accessed on July 7, 2014.

[2] Automotive Applications Council. AHSS 101-The Evolving Use of Advanced High-Strength Steels for Automotive Application. 2011. Available from http://www.autosteel.org. Accessed on April 20, 2014.

[3] SMDI. Lightweight Steel Wheel Executive Summary-AHSS Research. Available from http://www.autosteel.org. Accessed on July 15, 2014.

[4] X. Zhu, Z. Ma, L. Wang. Current Status of Advanced High Strength Steel for Auto-making and its Development in Baosteel. Available from http://www.baosteel.com. Accessed on May 21. 2014.

[5] D. Bhattacharya, An overview of advanced high strength steels (AHSS), Advanced High Strength Steel Workshop, Arlington, Virginia, USA (October 22-23, 2006).

[6] M.S. Rashid, B.V.N. Rao, Tempering Characteristics of a Vanadium Containing Dual Phase Steel, in: R.A. Kot, B.L. Bramfitt (Eds.) Fundamentals of Dual-Phase Steels, TMS-AIME, Warrendale, PA, 1981, pp. 246-264.

[7] R.A. Kot, J.W. Morris, Structure and Properties of Dual-Phase Steels, TMS AIME, Warrandale, PA, 1979.

[8] O. Bouaziz, H. Zurob, M. Huang, Driving Force and Logic of Development of Advanced High Strength Steels for Automotive Applications, Steel Research Int., 84 (2013) 937-947.

[9] A. Abraham. Future Growth of AHSS. *Great Designs in Steel Seminar*. May, 2011. Available from http://www.ducker.com. Accessed on July 17, 2014.

[10] E. Ghassemieh. Materials in Automotive Application, State of the Art and Prospects. Available from http://www.intechopen.com. Accessed on July 14, 2014.

[11] ULSAB-AVC Consortium. ULSAB-AVC (Advanced Vehicle Concepts) Overview Report. Available from http://www.autosteel.org. Accessed on April 12, 2014.

[12] ArcellorMittal. Usibor: Steels for Hot Stamping. Available from http://fce.arcelormittal.com. Accessed on April 12, 2014.

[13] R. Z. Mallen, S. Tarr, J. Dykeman. Recent Applications of High Strength Steels in North American Honda Production, Great Designs in Steel Seminar. Michigan, USA. Apr, 2008. Available from http://www.autosteel.org. Accessed on July 22, 2014.

[14] I. Han. Advanced High-Strength Steel Technologies in the 2014 Chevy Spark, General Motors, Great Designs in Steel 2014. Michigan, USA. May 2014. Available from http://www.autosteel.org. Accessed on April 12, 2014.

[15] R.P. Gangloff, Hydrogen assisted cracking of high strength alloys, in: I. Milne, R.O. Ritchie, B. Karihaloo (Eds.) Comprehensive structural integrity Vol. 6, Environmentally Assisted Fracture, Elsevier, 2003, pp. 31 - 101.

[16] S. Lynch, Hydrogen embrittlement phenomena and mechanisms, Corros. Rev., 30 (2012) 105-123.

[17] I.M. Bernstein, G.M. Pressouyre, The role of traps in the microstructural control of hydrogen embrittlement of steels, in: R.A. Oriani, J.P. Hirth, M. Smialowski (Eds.) Hydrogen degradation of ferrous alloys, Noyes Publication, New Jersey, USA, 1985, pp. 641-685.

[18] G. Lovicu, M. Bottazzi, F. D'Aiuto, M. De Sanctis, A. Dimatteo, C. Santus, R. Valentini, Hydrogen embrittlement of automotive advanced high-strength steels, Metall. Mater. Trans. A., 43 (2012) 4075-4087.

[19] J.H. Ryu, Y.S. Chun, C.S. Lee, H.K.D.H. Bhadeshia, D.W. Suh, Effect of deformation on hydrogen trapping and effusion in TRIP-assisted steel, Acta Mater., 60 (2012) 4085-4092.

[20] M. Koyama, E. Akiyama, K. Tsuzaki, Hydrogen embrittlement in a Fe-Mn-C ternary twinning-induced plasticity steel, Corros. Sci., 54 (2012) 1-4.

[21] M. Loidl, O. Kolk, S. Veith, T. Gobel, Characterization of hydrogen embrittlement in automotive advanced high strength steels, Mat.-wiss. u.Werkstofftech, 42 (2011).

[22] J.A. Ronevich, J.G. Speer, D.K. Matlock, Hydrogen embrittlement of commercially produced advanced high strength steels, SAE Int. J. Mater. Manuf., 3 (2010) 255-267.

[23] A.R. Troiano, The role of hydrogen and other interstitials in the mechanical behavior of metals, Trans. ASM, 52 (1960) 54 - 80.

[24] R.A. Oriani, A mechanistic theory of hydrogen embrittlement of steels, Ber. Bunsenges. Phys. Chem., (1972) 848 - 857.

[25] C.D. Beachem, A new model for hydrogen assisted cracking (Hydrogen embrittlement), Metall. Trans., 3 (1972) 437 – 451.

[26] H. K. Birnbaum, P. Sofronis, Hydrogen-enhanced localized plasticity-A mechanism for hydrogen related fracture, Mater. Sci. Eng. A, 176 (1994) 191-202

[27] A. Barnoush, H. Vehoff, Electrochemical nanoindentation: a new approach to probe hydrogen deformation interaction, Scripta Metall., 55 (2006) 185 - 198.

[28] S.P. Lynch, Environmentally assisted cracking: overview of evidence for an adsorption-induced localised-slip process, Acta Metall., 20 (1988) 2639 - 2661.

[29] A. Atrens, C.C. Brosnan, S. Ramamurthy, A. Oehlert, I.O. Smith, Linearly increasing stress test (LIST) for SCC research, Meas. Sci. Technol., 4 (1993) 1281-1292.

[30] W. Dietzel, A. Atrens, A. Barnoush, Mechanics of modern test methods and quantitative-accelerated testing for hydrogen embrittlement, in: R.P. Gangloff, B.P. Somerday (Eds.) Gaseous hydrogen embrittlement of materials in energy technologies, Woodhead Publishing Limited, 2012.

[31] N. Winzer, A. Atrens, W. Dietzel, G. Songa, K.U. Kainer, Comparison of the linearly increasing stress test and the constant extension rate test in the evaluation of transgranular stress corrosion cracking of magnesium, Mater. Sci. Eng. A, 472 (January 2008) 97-106.

[32] A. Atrens, A. Oehlert, Linearly-increasing-stress testing of carbon steel in 4 N $NaNO_3$ and on Bayer liquor, J Mater. Sci., 33 (1998) 783-788.

[33] E. Villalba, A. Atrens, Metallurgical aspects of rock bolt stress corrosion cracking, Mater. Sci. Eng. A, 491 (2008) 8-18.

[34] S. Ramamurthy, W.M.L. Lau, A. Atrens, Influence of the applied stress rate on the stress corrosion cracking of 4340 and 3.5NiCrMoV steels under conditions of cathodic hydrogen charging. , Corros. Sci., 53 (2011) 2419-2429.

[35] E. Gamboa, A. Atrens, Stress corrosion cracking fracture mechanisms in rock bolts, J Mater. Sci. , 38 (2003) 3813-3829.

[36] S. Ramamurthy, A. Atrens, Stress corrosion cracking of high-strength steels, Corros. Rev. , 31 (2013) 1-31.

[37] Q. Liu, B. Irwanto, A. Atrens, Influence of hydrogen on the mechanical properties of some medium-strength Ni–Cr–Mo steels, Mater. Sci. Eng. A, 617 (2014) 200-210.

[38] Q. Liu, B. Irwanto, A. Atrens, The Influence of Hydrogen on 3.5NiCrMoV steel studied using the linearly increasing stress test. , Corros. Sci., 67 (2013) 193-203.

[39] G. Vander Voort, Metallography, Principles and Practice, McGraw-Hill Publications, USA, 1984.

[40] R.D. Zipp, E.P. Dahlberg, Preparation and Preservation of Fracture Specimens, ASM Handbook, Vol 12: Fractography, (1987) 72-77.

[41] G. Krauss, Martensite in Steel: Strength and Structure, Mater. Sci. Engg. A, 273-275 (1999) 40-57.

[42] G. Krauss, Steels: Processing, Structure, and Performance, ASM International, USA, 2005.

[43] E.O. Hall, Yield Point Phenomena in Metals and Alloys, Plenum Press, New York, 1970.

[44] N. Bailey, Fisheyes, hydrogen embrittlement and removal, TWI Research Bulletin, 15 (December 1974).

[45] A.R. Marder, G. Krauss, The Morphology of Martensite in Iron-Carbon Alloys, Trans. ASM, 60 (1967) 651-660.

[46] M. Cohen, Martensitic Transformations in Materials Science and Engineering, Trans. JIM, 29 (1988) 609-624.

[47] D. Askeland, P. Fulay, V. Wright, The Science and Engineering of Materials, SI Edition, Cengage Learning, Canada, 2011.

[48] W. D. Callister, D. G. Rethwisch, Materials science and engineering: an introduction, eight ed., John Wiley and Sons, Inc, Hoboken, NJ, 2014.

[49] H. Matsuda, R. Mizuno, Y. Funakawa, K. Seto, S. Matsuoka, Y. Tanaka, Effects of auto-tempering behaviour of martensite on mechanical properties of ultra high strength steel sheets, J Alloy Compd., 5775 (2013) S661–S667.

[50] The Tempering of Martensite: Part One. Available from steel.keytometals.com/Articles/Art127. Accessed on September 2, 2014.

[51] G.E. Dieter, Mechanical Metallurgy, third ed., Mc-Graw Hill, London, 1986.

[52] M. Nagumo, Hydrogen embrittlement of steels turning of the research direction, Journal of the Iron and Steel Institute of Japan, 9 (2009) 222 - 227.

[53] H. Mohrbacher. Metallurgical optimization of martensitic steel sheet for automotive applications. Available from http://www.niobelcon.com. Accessed on April 10, 2014.

[54] A. Begic Hadzipasic, J. Malina, M. Malina, The Influence of Microstructure on Hydrogen Diffusion and Embrittlement of Multiphase Fine-Grained Steels withIncreased Plasticity and Strength, Chem. Biochem. Eng. Q., 25 (2011) 159-169.

[55] J.F. Bates, A.W. Loginow, Principles of Stress Corrosion Cracking As Related to Steels, Corrosion, 20 (1964) 189-197.

[56] A. Atrens, D. Mezzanote, N. Fiore, M. Genshaw, Electrochemical studies of hydrogen diffusion and permeability in Ni, Corros. Sci., 20 (1980) 673-684.

[57] Q. Liu, A. Atrens, Z. Shi, K. Verbeken, A. Atrens, Determination of the hydrogen fugacity during electrolytic charging, Corros. Sci., 87 (Oct 2014) 239-258.

[58] C. K. Gupta, Chemical metallurgy: principles and practice, Wiley-VCH, 2003.

[59] M. R. Louthan Jr, Hydrogen Embrittlement of Metals: A Primer for the Failure Analyst, J Fail. Anal. and Preven., 8 (2008) 289-307.

[60] L. Marchetti, E. Herms, P. Laghoutaris, J. Chene, Hydrogen embrittlement susceptibility of tempered 9%Cr-1%Mo steel, Int J Hydrogen Energ, 36 (2011) 15880-15887.

[61] P. Sofronis, A. Taha, Micromechanical Modeling of Hydrogen Transport- A Review, in: R.D. Kane (Ed.) Environmetally Assisted Cracking: Predictive Methods for Risk Assessment and Evaluation of Materials, Equipment and Structures, ASTM, PA, USA, 2000.

[62] M.A.V. Devanathan, Z.Stachurski, The mechanism of hydrogen evolution in iron in acid solutions by determination of permeation rates, J. Electrochem. Soc., 111 (1964) 619-623.

[63] T. Zakroczymski, Adaptation of the electrochemical permeation technique for studying entry, transport and trapping of hydrogen in metals, Electrochim. Acta, 51 (2006) 2261-2266.

[64] Q. Liu, A. Atrens, Reversible hydrogen trapping in a 3.5NiCrMoV medium strength steel, Corros. Sci., 96 (2015) 112-120.

[65] Jr. M.R. Louthan, Effects of hydrogen on the mechanical properties of low carbon and austenitic steels, in: I.M. Bernstein, A.W. Thompson (Eds.) Hydrogen in Metals, American Society for Metals, Metals Park, OH, pp. 53-77.

[66] T. Toh, W.M. Baldwin, Stress Corrosion Cracking and Embrittlement, J. Wiley and Sons, Inc., New York, USA., 1976.

[67] R.E. Smallman, R.J. Bishop, Modern Physical Metallurgy and Materials Engineering. 6th Ed., Elsevier Science Ltd., Woburn, MA, USA, 1999.

[68] M. Hashimoto, R.M. Latanision, The Role of Dislocations during Transport of Hydrogen in Hydrogen Embrittlement of Iron, Metall. Trans. A. , 19A (Nov 1988) 2799-2803.

[69] A. Turnbull, Test Methods for Environment-Assisted Cracking, in, National Physical Laboratory Report DMM(A)66, Teddington, Middlesex, UK, 1992.

[70] W. Gerberich, Modelling of hydrogen induced damage mechanisms in metals, in: R.P. Gangloff, B.P. Somerda (Eds.) Gaseous hydrogen embrittlement of materials in energy technologies, Woodhead, 2012, pp. 209-246.

[71] Y. Momotani, A. Shibata, D. Terada, N. Tsuji, Effect of Strain Rate on Hydrogen Embrittlement in Low Carbon Martensitic Steel, in: International Symposium on New Developments in Advanced High-Strength Sheet Steels, Vail, Colorado, USA. , June 2013.

[72] R.N. Parkins, Stress Corrosion Cracking-The Slow Strain Rate Technique, ASTM STP 665 (Philadelphia:American Society for Testing and Materials), (1979).

[73] T. Neeraj, R. Srinivasan, J. Li, Hydrogen embrittlement of ferritic steels: Observations on deformation microstructure, nanoscale dimples and failure by nanovoiding, Acta Mater., 60 (2012) 5160-5171.

[74] S.P. Lynch, Mechanism of hydrogen-assisted cracking- A review, in: N.R. Moody, A.W. Thomson, R.E. Ricker, G.W. Was, R.H. Jones (Eds.) Hydrogen effects on materials behaviour and corrosion deformation interactions, TMS, 2003.

[75] M.S. Walp, A. Wurm, J.F. Siekirk II, A.K. Desai, Shear Fracture in Advanced High Strength Steels, SAE Technical Paper # 2006-01-1433. SAE World Congress. Michigan, USA., (2006).

[76] S. Huang, Y. Zhao, C. He, Shear fracture of advanced high strength steels, J Iron Steel Res Int, 21 (2014) 938-944.

[77] Y. Li, M. Luo, J. Gerlach, T. Wierzbicki, Prediction of shear-induced fracture in sheet metal forming, J Mater. Proc. Tech., 210 (2010) 1858-1869.

[78] R.H. Wagoner, Shear Fracture of Advanced High Strength Steels (AHSS), in: The 8th Pacific Rim International Congress on Advanced Materials and Processing. Symposium Advanced Steels and Processing, PRICM, Hawaii, 2013.

[79] J.H. Kim, J. H. Sung, D. K. Matlock, D. Kim, R. H. Wagoner, Finite element and analytical study of plane strain draw-bend failure of advanced high strength steels, Int. J. Mater. Form, 3 (2010) 187-190.

[80] M. Moser, V. Schmidt. Fractography and mechanism of hydrogen cracking-The fisheye concept. Available from www.martin-moeser.de. Accessed on July 20, 2014.

[81] B. Strnadel, Failure of steels caused by hydrogen induced microcracks, Eng. Fracture Mech., 61 (1998) 299-310.

Table 1. Chemical composition (in wt %) and mechanical properties of the MS-AHSS.

Steel designation	C	Si	Mn	Al	Nb	Ti	Cr	Yield stress, MPa	Tensile stress, MPa	Elongation at fracture, e_f, %
MS980	0.117	0.38	1.639	0.034	0.014	0.038	0.014	883	1070	5
MS1180	0.159	0.399	1.625	0.027	0.013	0.026	0.020	1176	1355	3
MS1300	0.156	0.402	1.654	0.038	0.014	0.028	0.014	1185	1380	2.5
MS1500	0.192	0.385	1.495	0.034	0.014	0.028	0.024	1361	1667	2.9

Table 2. Results of stereological analysis of MS-AHSS.

Steel Designation	Ferrite		Martensite	
	Relative amount, %	Grain size, μm	Relative amount, %	Grain size, μm
MS980	30%	5-10	70%	5-20
MS1180	16%	< 5	84%	5-15
MS1300	10%	5-8	90%	10-20
MS1500	8%	< 3	92%	5-10

Table 3. LIST results for MS-AHSS; S represents 0.1 M NaOH solution.

Specimen designation	Environment	Potential, $V_{Ag/AgCl}$	Applied stress rate, MPA s^{-1}	Apparent threshold stress σ_{TH}, or yield stress, σ_y, MPa (±5)	Fracture stress, UTS, σ_f, MPa (±2)	Reduction in area, R_A, %	Hydrogen embrittlement index, I	Remarks
MS980-A-S	Air	n/a	UTM	883	1070			
MS980-A-300	Air	n/a	0.64	900	1120	69		Ductile; necking and cup-and-cone fracture evident.
MS980-A-30	Air	n/a	0.064	880	1106	66		Ductile; necking and cup-and-cone fracture evident.
MS980-H1.2-30	S	-1.200	0.064	880	1086	67	0	Ductile; necking and cup-and-cone fracture evident.
MS980-H1.5-30	S	-1.500	0.064	880	1090	67	0	Ductile; necking and cup-and-cone fracture evident.
MS980-H1.8-30	S	-1.800	0.064	860	1084	66	0	Ductile; necking and cup-and-cone fracture evident.
MS980-H1.2-3	S	-1.200	0.0064	870	1064	64	3	Ductile; necking and cup-and-cone fracture evident.
MS980-H1.5-3	S	-1.500	0.0064	880	1058	64	3	Ductile; necking and cup-and-cone fracture evident.
MS980-H1.8-3	S	-1.800	0.0064	820	1040	47	29	Necking was present; shear-type fracture evident. Surface cracks near fracture.
MS1180-A-S	Air	n/a	UTM	1176	1355			
MS1180-A-300	Air	n/a	0.54	1170	1352	69		Ductile; necking and cup-and-cone fracture evident.
MS1180-A-30	Air	n/a	0.054	1150	1386	67		Ductile; necking and cup-and-cone fracture evident.
MS1180-H1.2-30	S	-1.200	0.054	1150	1382	66	2	Ductile; necking and cup-and-cone fracture evident.
MS1180-H1.5-30	S	-1.500	0.054	1145	1384	66	2	Ductile; necking and cup-and-cone fracture evident.
MS1180-H1.8-30	S	-1.800	0.054	1140	1378	55	18	Necking present; cup and cone fracture evident. Surface cracks in the necked portion.
MS1180-H1.2-3	S	-1.200	0.0054	1140	1346	58	13	Necking present. Surface cracks in the necked portion.
MS1180-H1.5-3	S	-1.500	0.0054	1080	1328	33	51	Little necking; shear-type fracture evident. Surface cracks near fracture lip.

MS1180-H1.8-3	S	-1.800	0.0054	1055	1340	22	67	Little necking volume; shear-type fracture evident. Surface cracks seen near fracture.
MS1300-A-S	Air	n/a	UTM	1185	1380			
MS1300-A-300	Air	n/a	0.80	1150	1450	62		Ductile; necking and cup-and-cone fracture evident.
MS1300-A-30	Air	n/a	0.080	1160	1436	62		Ductile; necking and cup-and-cone fracture evident.
MS1300-A-3	Air	n/a	0.0080	1150	1424	62		Ductile; necking and cup-and-cone fracture evident.
MS1300- H1.2-30	S	-1.200	0.080	1120	1430	41	34	Signs of necking present. Shear-type fracture. Surface cracks at the neck area.
MS1300-H1.5-30	S	-1.500	0.080	1110	1432	31	50	Signs of necking present. Shear-type fracture. Surface cracks at neck area.
MS1300-H1.8-30	S	-1.800	0.080	1075	1388	29	53	Necking barely noticeable. Shear-type fracture. Surface cracks present near fracture.
MS1300-H1.8-3	S	-1.800	0.0080	1030	1362	21	66	Necking is absent; shear-type fracture evident. Surface cracks near fracture.
MS1300-H1.8-30-L	S	-1.800	0.080	1080	1380	32	51	Necking barely noticeable. Shear-type fracture. Surface cracks present near fracture.
MS1500-A-S	Air	n/a	UTM	1361	1667			
MS1500-A-300	Air	n/a	0.80	1340	1678	61		Ductile; necking and cup-and-cone fracture evident.
MS1500-A-30	Air	n/a	0.080	1340	1678	60		Ductile; necking and cup-and-cone fracture evident.
MS1500- H1.2-30	S	-1.200	0.080	1285	1654	28	53	Signs of necking present. Mixed cup-cone and shear-type fracture. Surface cracks at neck area.
MS1500-H1.5-30	S	-1.500	0.080	1280	1648	20	67	Necking barely noticeable. Shear-type fracture. Surface cracks present near fracture.
MS1500-H1.8-30	S	-1.800	0.080	1225	1646	18	70	Necking barely noticeable. Shear-type fracture. Surface cracks present near fracture.
MS1500-H1.8-3	S	-1.800	0.0080	1020	1570	12	80	Necking is absent; shear-type fracture evident. Small surface cracks near fracture.

Table 4 Summary of fractography. D is ductile cup-and-cone type fracture. S is shear fracture. An intermediate applied stress rate of 0.06 MPa s^{-1} is equivalent to a strain rate of 3 x 10^{-7} s^{-1} in the elastic loading region. The lowest stress rate of 0.006 MPa s^{-1} is equivalent to a strain rate of 3 x 10^{-8} s^{-1} in the elastic loading region.

	Intermediate stress rate		
Specimen	-1200 $mV_{Ag/AgCl}$	-1500 $mV_{Ag/AgCl}$	-1800 $mV_{Ag/AgCl}$
MS980	D	D	D
MS1180	D	D	D
MS1300	S	S	S
MS1500	S	S	S

	Lowest stress rate		
Specimen			
MS980	D	D	S
MS1180	D	S	S
MS1300	S	S	S
MS1500	S	S	S